

Analytic approach to thermoelectric transport in double quantum dots

Nahual Sobrino,^{1,2,*} David Jacob,^{1,3,4} and Stefan Kurth^{1,3,5}

¹*Nano-Bio Spectroscopy Group and European Theoretical Spectroscopy Facility (ETSF),
Departamento de Polímeros y Materiales Avanzados: Física,
Química y Tecnología, Universidad del País Vasco UPV/EHU,
Avenida de Tolosa 72, E-20018 San Sebastián, Spain*

²*The Abdus Salam International Center for Theoretical Physics (ICTP), Strada Costiera 11, 34151 Trieste, Italy*

³*IKERBASQUE, Basque Foundation for Science, Plaza Euskadi 5, E-48009 Bilbao, Spain*

⁴*Departamento de Física Aplicada, Universidad de Alicante,
Campus de San Vicente del Raspeig, E-03690 Alicante, Spain*

⁵*Donostia International Physics Center (DIPC),
Paseo Manuel de Lardizabal 4, E-20018 San Sebastián, Spain*

(Dated: January 30, 2025)

A recently proposed analytical solution for the equations of motion of the one-body Green function of the double quantum dot is extended to the out-of-equilibrium situation. By solving a linear system for the density correlators, not only the local occupations but also charge and heat currents as well as transport coefficients and the figure of merit are analytically derived in terms of system parameters and external driving forces. The emerging regions of stable occupation and finite currents are explained in terms of addition and removal energies, corresponding to the poles of the Green function. The analytical results are validated against the hierarchical equations of motion method, showing excellent agreement.

I. INTRODUCTION

The study of thermoelectric transport in nanoscale systems is a rapidly advancing field, driven by the exploration of quantum effects in low-dimensional systems, the need for efficient energy conversion technologies, and advancements in nanofabrication techniques, among others [1–8]. In this context, quantum dots (QDs) have gained significant research interest due to their nanoscale dimensions, discrete energy levels, and highly tunable electronic properties [9–12]. Double quantum dots (DQDs), in particular, offer additional control over electronic states through interdot coupling and Coulomb repulsion, which allows for the manipulation of charge and spin states, coherence effects, and enhanced interaction dynamics, making them promising candidates for thermoelectric applications [13–19].

While much research has traditionally focused on the equilibrium properties of DQDs [20–24], these studies, although very useful and interesting, do not capture the full complexity of these systems under practical operating conditions. In real-world applications, devices often operate under nonequilibrium conditions, influenced by external driving forces such as thermal gradients and bias voltages. Understanding the behavior of DQDs in these out-of-equilibrium situations is crucial for optimizing their performance in thermoelectric devices and other nanoscale applications [25–40].

Various theoretical techniques have been developed to solve non-equilibrium open quantum systems, including the Hierarchical Equations of Motion (HEOM), Numerical Renormalization Group (NRG), Quantum Master

Equations (QME), and Dynamical Mean-Field Theory (DMFT) [41–46]. Among these, the equation of motion (EOM) method stands out as a powerful technique that provides a systematic approach to deriving the equations governing the dynamics of Green functions (GFs) in Hubbard and impurity models [47–51]. The EOM technique has successfully been applied to single and multiple QD systems, allowing for a numerical evaluation of the system's GF in equilibrium and non-equilibrium situations [52–58]. Given the complex structure of the equations, the solution is typically obtained through a self-consistent numerical procedure. Recently, an alternative fully analytical derivation of the EOM for the DQD in the Coulomb blockade regime at thermal equilibrium has been proposed in Ref. [59]. This approach provides explicit functional dependencies that are crucial for understanding the underlying physical mechanisms governing orbital occupations and spectra, both of which are essential for designing efficient nanoscale devices.

Here we extend the analytical derivations to the nonequilibrium situation and obtain expressions for key quantities such as orbital occupations, charge and heat currents, and transport coefficients in terms of the system parameters. These expressions will enable us to systematically study the influence of these parameters and external driving forces on the thermoelectric characteristics of DQDs.

The rest of the paper is organized as follows: In Section II, we introduce the DQD Hamiltonian coupled to reservoirs, and derive the expressions for charge and heat currents using the EOM approach followed by the transport coefficients and the figure of merit. In Section III, we present our results and validate them against HEOM numerical simulations. Finally, Section IV concludes the paper with a summary of our findings.

* nsobrino@ictp.it

II. MODEL AND CURRENTS FROM THE EQUATIONS OF MOTION

A. Double Quantum Dot Hamiltonian

We consider a parallel double quantum dot system attached to two electron reservoirs. The reservoirs are in local thermal equilibrium with temperatures T_L and T_R , and chemical potentials μ_L and μ_R , respectively. The Hamiltonian of the system is given by

$$\hat{\mathcal{H}} = \hat{\mathcal{H}}_0 + \sum_{i\alpha k\sigma} \epsilon_{\alpha ki} \hat{c}_{\alpha ki\sigma}^\dagger \hat{c}_{\alpha ki\sigma} + \sum_{i\alpha k\sigma} \left(V_{\alpha ki} \hat{c}_{\alpha ki\sigma}^\dagger \hat{d}_{i\sigma} + \text{H.c.} \right), \quad (1)$$

where

$$\hat{\mathcal{H}}_0 = \sum_i v_i \hat{n}_i + \sum_i U_i \hat{n}_{i\sigma} \hat{n}_{i\bar{\sigma}} + U_{12} \hat{n}_1 \hat{n}_2 \quad (2)$$

describes the isolated double dot. Here, $\hat{d}_{i\sigma}^\dagger$ ($\hat{d}_{i\sigma}$) is the creation (annihilation) operator for an electron with spin σ on dot i . $\hat{c}_{\alpha ki\sigma}^\dagger$ ($\hat{c}_{\alpha ki\sigma}$) is the creation (annihilation) operator for an electron with spin σ in state k of lead α coupled to the site i . Moreover, v_i and U_i are the on-site energy and the intra-Coulomb repulsion of dot i , respectively, while U_{12} is the inter-Coulomb repulsion between the two dots. The total and spin-resolved density operators are defined as $\hat{n}_i = \sum_{\sigma=\uparrow,\downarrow} \hat{n}_{i\sigma}$ and $\hat{n}_{i\sigma} = \hat{d}_{i\sigma}^\dagger \hat{d}_{i\sigma}$, respectively. The last two terms in Eq. (1) describe the single-particle eigenstates of the isolated reservoirs and the tunneling between the dots and the two reservoirs $\alpha = L, R$, with $V_{\alpha ki}$ as the coupling parameter. In the following, we work in the wide band limit, i.e., the reservoirs are featureless leads at chemical potential μ_α and the hybridization function or embedding self-energy $\Delta_i^\alpha \equiv \sum_k |V_{\alpha ki}|^2 / (\omega - \epsilon_{\alpha ki})$ becomes energy-independent. Additionally, we focus on the situation where both dots couple to the leads with the same coupling strength γ_α so that $\Delta_i^\alpha = -i\gamma_\alpha/4$. The system can be brought out of equilibrium by imposing a thermal gradient $\Delta T = T_L - T_R$ and/or an external DC bias $V = \mu_L - \mu_R$ across the junction. It is assumed that, in the long-time limit, these perturbations result in a steady-state with an electrical current (I) and energy and heat currents (W and Q , respectively).

In the following, we use the sign convention that currents flowing into the central region are positive. Due to the conservation of charge and energy, the steady-state electrical/energy current entering from the left lead equals the steady-state electrical/energy current exiting through the right lead, i.e., $I \equiv I_L = -I_R$ (electrical current), $W \equiv W_L = -W_R$ (energy current), and $Q \equiv Q_L = P - Q_R$ (heat current) where $P = -IV$ is the electrical power. Furthermore the energy current of lead α is related to the charge and heat currents as $W_\alpha = Q_\alpha + \mu_\alpha I_\alpha$.

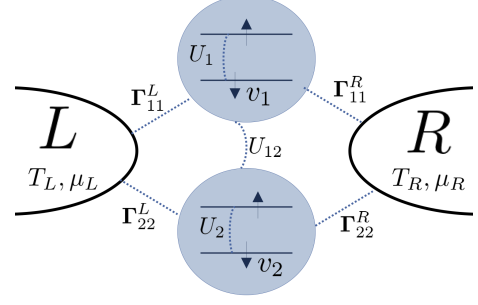


FIG. 1. Schematic representation of the transport setup for the DQD. The leads are coupled to the dots with the same coupling strength $\Gamma_{ij}^\alpha = \delta_{ij} \gamma_\alpha/2$.

B. Charge and Heat Currents from the Equation of Motion Approach

The charge and heat currents through an interacting region attached to two non-interacting electronic reservoirs can be derived using the non-equilibrium Keldysh formalism [51, 60] ($f \equiv \int \frac{d\omega}{2\pi}$ in the following):

$$I = \frac{i}{2} \int [\text{Tr} \{ (f_L(\omega) \mathbf{\Gamma}^L - f_R(\omega) \mathbf{\Gamma}^R) (\mathbf{G}^r(\omega) - \mathbf{G}^a(\omega)) \} + \text{Tr} \{ (\mathbf{\Gamma}^L - \mathbf{\Gamma}^R) \mathbf{G}^<(\omega) \}] , \quad (3a)$$

$$Q = \frac{i}{2} \int (\omega - V_L) [\text{Tr} \{ (f_L(\omega) \mathbf{\Gamma}^L(\omega) - f_R(\omega) \mathbf{\Gamma}^R) \times (\mathbf{G}^r(\omega) - \mathbf{G}^a(\omega)) \} + \text{Tr} \{ (\mathbf{\Gamma}^L - \mathbf{\Gamma}^R) \mathbf{G}^<(\omega) \}] , \quad (3b)$$

where $f_\alpha(\omega) = [1 + e^{\frac{\omega - \mu_\alpha}{T_\alpha}}]^{-1}$ is the Fermi distribution of lead $\alpha = L, R$. The retarded $\mathbf{G}^r(\omega)$, advanced $\mathbf{G}^a(\omega)$, and lesser $\mathbf{G}^<(\omega)$ Green functions (GF) are the Fourier transforms of the matrices with elements $G_{ij}^r(t) = -i\theta(t) \langle \{ \hat{d}_i(t), \hat{d}_j^\dagger(0) \} \rangle$, $G_{ij}^a(t) = i\theta(-t) \langle \{ \hat{d}_i(t), \hat{d}_j^\dagger(0) \} \rangle$, and $G_{ij}^<(t) = i \langle \hat{d}_i^\dagger(0) \hat{d}_j(t) \rangle$, respectively, with $\theta(t)$ as the Heaviside step function, and the brackets $\langle \dots \rangle$ indicating thermal average. $\mathbf{\Gamma}^\alpha$ are the so-called coupling matrices describing the coupling of the DQD to each of the leads, and defined as the anti-hermitian part of the embedding self-energies, defined above. Here the embedding-self energies and thus the coupling matrices are diagonal in the dot indices i , and hence $\Gamma_{ij}^\alpha = -2 \text{Im} \Delta_i^\alpha \delta_{ij}$. In the symmetrically coupled situation, $\Gamma_{ij}^\alpha = \delta_{ij} \gamma_\alpha/2$, considered here, the currents through the DQD system of Eq. (1) simplify to

$$I = -\frac{\gamma}{2} \sum_i \int (f_L(\omega) - f_R(\omega)) \text{Im}(G_i^r(\omega)) , \quad (4a)$$

$$Q = -\frac{\gamma}{2} \sum_i \int (\omega - V_L) (f_L(\omega) - f_R(\omega)) \text{Im}(G_i^r(\omega)) . \quad (4b)$$

The equation-of-motion (EOM) approach allows for the calculation of the one-particle GF in terms of higher order GFs whose EOM in turn generates yet higher order GFs. In order for the EOMs to be practically useful, this hierarchy needs to be truncated. Here we employ the (approximate) truncation scheme of Ref. [59] which may be generalized with the same arguments to the out-of-equilibrium steady state situation. Our truncation scheme may be rationalized in three different ways [59], all leading to the same approximation. One of these rationalizations neglects certain higher-order GFs but the same result can also be achieved by simply broadening all poles (see below) of all GFs by the coupling parameter $\gamma = \gamma_L + \gamma_R$. Finally, the assumption that the local density operator and the Hamiltonian commute, i.e., $[\hat{n}_{i\sigma}, \mathcal{H}] \approx 0$ also leads to the same truncation scheme. This approximation is accurate in the Coulomb blockade regime, when the temperature kT is large compared to the broadening $-\text{Im}\Delta_i$ by the reservoirs. Furthermore, we approximate the correlators in the out-of-equilibrium situation by the phenomenological expression [58, 61–63]

$$\langle n_{i'\sigma'} \dots n_{i''\sigma''} n_{i'''\sigma'''} \rangle = - \int \tilde{f}(\omega) \times \text{Im} \left(\langle \langle n_{i'\sigma'} \dots n_{i''\sigma''} d_{i'''\sigma'''}^\dagger : d_{i'''\sigma'''}^\dagger \rangle \rangle \right), \quad (5)$$

where $\tilde{f}(\omega) = \frac{1}{2}(f_L(\omega) + f_R(\omega))$. This is a straightforward generalization of the corresponding (exact) equilibrium expression (see [59]) to which it correctly reduces in thermal equilibrium. In particular, the one-body correlators correspond to the local occupation

$$\langle n_{i\sigma} \rangle = - \int \tilde{f}(\omega) \text{Im} (G_{i\sigma}^r(\omega)) . \quad (6)$$

Eq. (5) is an approximation in the out-of-equilibrium situation.

In Ref. [59], we derived an analytical expression for the single-particle GF at equilibrium for the DQD system given by Eq. (1). With the assumption Eq. (5) for the non-equilibrium correlators this derivation can be transferred one-to-one to the non-equilibrium situation considered here, resulting in an expression for the GF solely in terms of the occupations $\langle \hat{n}_i \rangle$ of each QD i and the electron addition and removal energies

$$G_{i\sigma}^r(\omega) = \sum_{j=1}^6 \frac{r_{i,j}}{\omega - p_{i,j} + i\frac{\gamma}{2}}, \quad (7)$$

where the poles $p_{i,j}$ correspond to the addition and removal energies

$$\begin{aligned} p_{i,1} &= v_i, & p_{i,4} &= v_i + U_i + 2U_{12}, \\ p_{i,2} &= v_i + U_i, & p_{i,5} &= v_i + U_{12}, \\ p_{i,3} &= v_i + U_i + U_{12}, & p_{i,6} &= v_i + 2U_{12}, \end{aligned} \quad (8)$$

and the residues $r_{i,j}$ are linear combinations of the local occupations (see Eq. (23) of Ref. [59]), but computed

via the non-equilibrium expression Eq. (6) instead of the equilibrium one. The residues and the densities expressions analytically derived in Ref. [59] depend on a function $\phi(p)$ that corresponds to the integral of a single pole in the complex plane multiplied by the Fermi distribution. In the out of equilibrium situation, the explicit dependence on the local chemical potentials and temperatures of each of the leads in Eq. (5), make the results completely analogous to the equilibrium situation with the modified function $\phi(p)$ which now reads:

$$\phi(p) = \int \tilde{f}(\omega) \frac{\gamma}{(\omega - p)^2 + \frac{\gamma^2}{4}} = \frac{1}{2} - \sum_{\alpha} \frac{1}{2\pi} \text{Im}[\psi(z_{\alpha})], \quad (9)$$

where $z_{\alpha} = \frac{1}{2} + \frac{\gamma/2 + i(p - V_{\alpha})}{2\pi T_{\alpha}}$ for $\alpha = L, R$, and $\psi(z) = \frac{d \log(\Gamma(z))}{dz}$ is the digamma function with general complex argument z , and $\Gamma(z)$ is the gamma function.

Given the structure of the GF as a sum of single poles in the complex plane, the current integrals Eq. (4b) can also be computed analytically [64], leading to the expressions

$$I = - \frac{\gamma}{2\pi} \sum_{i,j,\alpha} s_{\alpha} r_{i,j} \text{Im}[\psi(z_{i,j}^{\alpha})], \quad (10a)$$

$$\begin{aligned} Q &= \frac{\gamma}{2\pi} \sum_{i,j,\alpha} s_{\alpha} r_{i,j} \left[\frac{\gamma}{2} \text{Re}[\psi(z_{i,j}^{\alpha})] - (p_{i,j} - \frac{V}{2}) \text{Im}[\psi(z_{i,j}^{\alpha})] \right] \\ &+ \frac{\gamma^2}{2\pi} \log \left(\frac{T_L}{T_R} \right), \end{aligned} \quad (10b)$$

with $s_{\alpha} = \pm 1$ for $\alpha = L, R$, and $z_{i,j}^{\alpha} = \frac{1}{2} + \frac{\gamma/2 + i(p_{i,j} - V_{\alpha})}{2\pi T_{\alpha}}$.

C. Linear Transport coefficients

The linear response relationship between the currents and the external potentials reads

$$\begin{pmatrix} I \\ Q \end{pmatrix} = \begin{pmatrix} L_{11} & L_{12} \\ L_{21} & L_{22} \end{pmatrix} \begin{pmatrix} V/T \\ \Delta T/T^2 \end{pmatrix}, \quad (11)$$

with $L_{12} = L_{21}$ from Onsager's relation [65]. Taking the derivatives in Eq. (10) with respect to the external potentials, we can analytically derive the matrix elements L_{ij} of the conductance matrix as

$$L_{11} = T \left. \frac{\partial I}{\partial V} \right|_{\substack{V=0 \\ \Delta T=0}} = \frac{\gamma}{4\pi^2} \sum_{i,j} r_{i,j} \text{Im}[i\psi'(z_{i,j})], \quad (12a)$$

$$L_{12} = T^2 \left. \frac{\partial I}{\partial \Delta T} \right|_{\substack{V=0 \\ \Delta T=0}} = \frac{\gamma}{4\pi^2} \sum_{i,j} r_{i,j} \text{Im}[l_{i,j}^0 \psi'(z_{i,j})], \quad (12b)$$

$$\begin{aligned} L_{22} &= T^2 \left. \frac{\partial Q}{\partial \Delta T} \right|_{\substack{V=0 \\ \Delta T=0}} = \frac{\gamma}{4\pi^2} \sum_{i,j} r_{i,j} [p_{i,j} \text{Im}[l_{i,j}^0 \psi'(z_{i,j})] \\ &- \frac{\gamma}{2} \text{Re}[l_{i,j}^0 \psi'(z_{i,j})]] + \frac{\gamma^2 T}{2\pi}, \end{aligned} \quad (12c)$$

where $l_{i,j}^0 = \frac{\gamma}{2} + ip_{i,j}$, $z_{i,j} = \frac{1}{2} + \frac{l_{i,j}^0}{2\pi T}$, and $\psi'(z) = \frac{d^2 \log(\Gamma(z))}{dz^2}$ is the trigamma function with complex argument z . [66] The linear transport coefficients, i.e., the electrical conductance \mathcal{G} , the Seebeck coefficient \mathcal{S} and the thermal conductance κ , can be expressed in terms of the conductance matrix elements L_{ij} as

$$\mathcal{G} = \left. \frac{\partial I}{\partial V} \right|_{\substack{V=0 \\ \Delta T=0}} = \frac{L_{11}}{T}, \quad (13a)$$

$$\mathcal{S} = - \left. \frac{\partial V}{\partial \Delta T} \right|_{\substack{I=0 \\ Q=0}} = \frac{L_{12}}{TL_{11}}, \quad (13b)$$

$$\kappa = \left. \frac{\partial Q}{\partial \Delta T} \right|_{\substack{I=0 \\ Q=0}} = \frac{1}{T^2} \left(L_{22} - \frac{L_{12}^2}{L_{11}} \right). \quad (13c)$$

From Eq. (13) one can compute the dimensionless figure of merit ZT , a key parameter in evaluating the efficiency of thermoelectric materials. It provides a measure of the system's ability to convert heat into electricity

$$ZT = \frac{\mathcal{S}^2 \mathcal{G} T}{\kappa}. \quad (14)$$

For a system to have efficient thermoelectric properties, we desire ZT to be as high as possible, which implies a high Seebeck coefficient, high electrical conductance, and low thermal conductance. The thermal conductance, κ , consists of the electronic part, κ_e , and the phonon part, κ_{ph} . In our analysis, the phonon contribution, which arises from phonon transport through the device, has been neglected. Therefore, the ZT values calculated by excluding the phonon thermal conductivity represent the upper limits for each set of parameters.

III. RESULTS

In this section, we implement the analytical EOM method to calculate densities, currents, transport coefficients and the figure of merit of the DQD across various regimes determined by the interaction parameters (see Ref. [67]). We validate our findings by comparing them with the numerical hierarchical equations of motion (HEOM) approach [41]. A Python implementation of our EOM method for the DQD is available on GitHub[68].

In Fig. 2, we show the residues $r_{1,j}$ of the GF (panels (a-c)) given by Eq. (23) of Ref. [59] evaluated with $\phi(p)$ from Eq. (9) and the stability diagrams (panels (d-f)) of the DQD system under varying gate voltages v_1 and v_2 , and for different applied bias voltages between the electrodes V for interaction parameters $U_1 = 2, U_2 = 3, U_{12} = 1$. The stability diagrams represent regions in the $v_1 - v_2$ plane where the occupation numbers are stable, i.e., they do not fluctuate in the limit of low temperature and weak coupling to the reservoirs. The lines separating regions in the stability diagrams correspond to parameters which lead to degenerate ground states.

In the low temperature and low coupling limit and at $V = 0$ (Fig. 2 left), each residue has a finite contribution in a maximum of two different regions of the stability diagram. For fixed (v_1, v_2) , either only one non-vanishing residue with value 1 exists, or there exist two non-vanishing residues both with value 0.5 (in the limit of low temperature and weak coupling). This implies that the local spectral function on dot 1 has either one or two poles. At $V = 0$, the occupations in the different regions of the stability diagram are stable at integer values.

When a finite symmetric bias voltage is applied between the electrodes, the vertical and horizontal lines separating the different regions of the stability diagram in the (v_1, v_2) plane split, defining new regions with fractional occupations in the stability diagram. This splitting can be understood by the local bias dependencies in the two Fermi functions \tilde{f} of Eq. (9). In the stripe region, a given pole with finite residue in this region (see top panels of Fig. 2), will fall between the local chemical potentials $\mu + V_\alpha$ ($\alpha = L, R$) entering \tilde{f} . Alternatively, one can understand the formation of the stripe regions in the finite-bias stability diagrams by performing a variable substitution $\omega' = \omega - V_\alpha$ separately for each of the Fermi functions contributing to \tilde{f} of Eq. (9). Then the contributions of the poles of the GF of site i will be shifted to an effective gate level $v'_i = v_i - V_\alpha$. The width of these new regions exactly corresponds to the value of the applied voltage $V = V_L - V_R$, and they are centered around lines separating regions of the $V = 0$ stability diagram. In the case of an asymmetric bias, the new stripe regions are shifted asymmetrically with respect to the degeneracy lines (not shown).

In (Fig. 2(b)), where $V = 0.5 = 2V_L = -2V_R$, the values of the residues along the stripe regions is either 0.75 or 0.25. In the corresponding stability diagram, the stripes correspond to stable regions of non-integer local occupation of one of the sites with values $2/3$ or $4/3$. This value can be deduced from the zero-bias degeneracy line from which the new stripe region originates. If the two regions separated by this degeneracy line (at equilibrium) have occupancy in one of the sites n_i equal to 0 and 1, then the finite stripe region will have occupation $n_i = 2/3$. On the other hand, if the two differing occupations for n_i are 1 and 2 then the stripe region will have occupation $n_i = 4/3$. The values $2/3$ and $4/3$ for the fractional occupations at finite bias also appear in the single-impurity Anderson model at finite bias [69]. As the bias is increased further to $V = 1$ (Fig. 2(c)), the new width of the stripe regions of both the residues and the stability diagram increase according to the bias value. When the new vertical and horizontal stripe regions meet at a triple degenerate point, further new square regions are created in both the residues and the stability diagram. This results from the increased splitting and mixing of energy levels due to the higher bias voltage, leading to more complex patterns of electron occupation.

In Fig. 3, the local occupations n_i and charge current I (insets) are shown for specific gate potentials, corre-

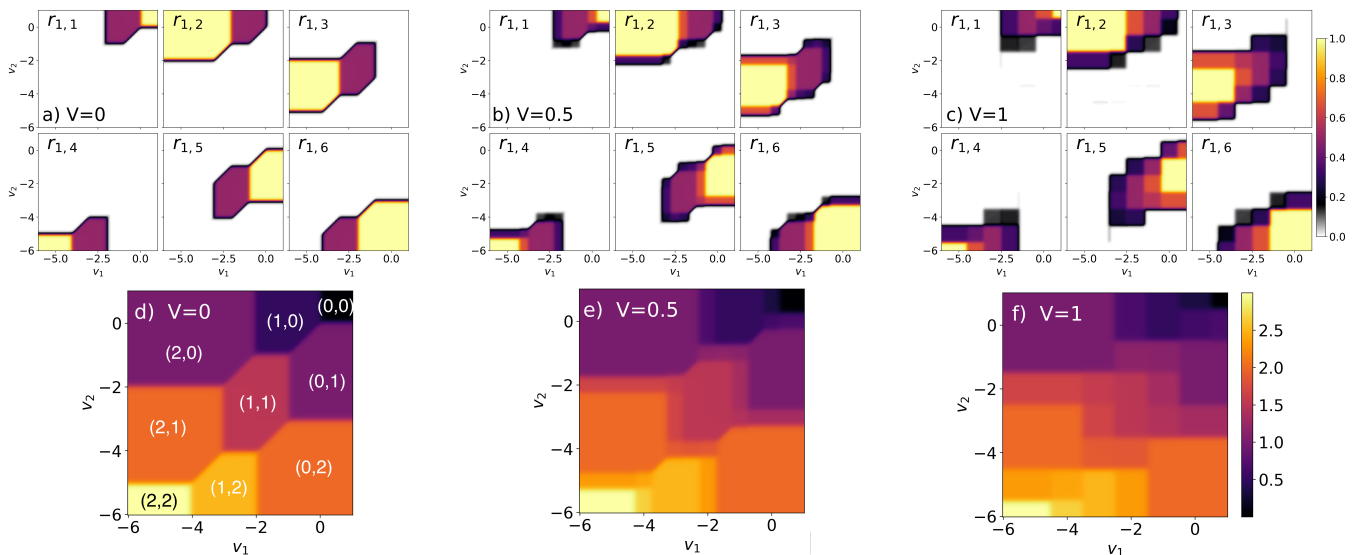


FIG. 2. Residues $r_{1,j}$ of the Green function (top row) and stability diagrams (bottom row) as functions of gate potentials v_i for different symmetrically applied bias voltages V . Panels (a) and (d) correspond to $V = 0$, panels (b) and (e) correspond to $V = 0.5$, and panels (c) and (f) correspond to $V = 1$. In panel (d) we also indicate the occupations (n_1, n_2) for different regions of the stability diagram. The parameters used are $U_1 = 2$, $U_2 = 3$, $T = 0.05$, and $\gamma \rightarrow 0$. Energies in units of U_{12} .

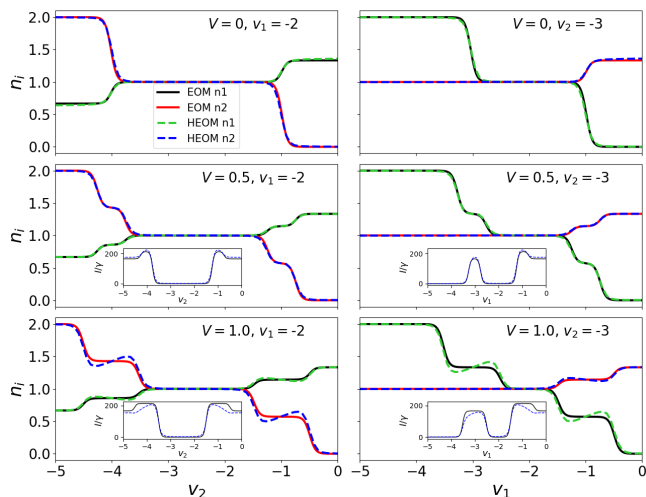


FIG. 3. Local occupations n_i as functions of gate levels v_2 (left panels) and v_1 (right panels) for different bias voltages V . The insets show a comparison between the EOM (solid black) and the HEOM (dashed blue) charge currents. The interactions and parameters considered are $U_1 = 2$, $U_2 = 3$, $T = 0.05$, and $\gamma = 0.01$. Energies in units of U_{12} .

sponding to vertical and horizontal line cuts of the stability diagrams shown in Fig. 2. These plots provide a detailed examination of how the occupations change with varying bias voltages at fixed interaction values. The left panels of Fig. 3 show the occupations n_i as function of the gate voltage v_2 at $v_1 = -2$, while the right panels present the occupations as functions of v_1 at $v_2 = -3$. At $V = 0$ and fixed $v_1 = -2$, the occupations evolve as v_2

varies, with the main structure featuring three plateaus and two step transitions at $v_2 = -4$ and $v_2 = -1$. The non-integer values of n_1 correspond to the degenerate energy lines separating the regions in the stability diagram of Fig. 2(d). Similarly, at fixed $v_2 = -3$, n_1 evolves with steps at $v_1 = -3$ and $v_1 = -1$. In contrast, n_2 does not exhibit a step at $v_1 = -3$, as this transition corresponds to the ground state change from $(2, 1)$ to $(1, 1)$ in the low temperature limit. For $v_1 > -1$, the second dot is along a degenerate line, resulting in non-integer n_2 . When a finite bias voltage of $V = 0.5$ is applied (central panels), an additional plateau appears between the other plateaus, indicating the influence of the bias on the poles. The width of this new feature exactly corresponds to the applied bias, with an occupation corresponding to the value of half the occupation at the center of the step in the $V = 0$ situation. When the bias voltage increases to $V = 1$ (lower panels), the additional plateaus in occupations further broaden, corresponding to the new vertical and horizontal regions in the stability diagram (see Fig. 2(f)). At relatively small bias, the analytical occupations and the charge current obtained from the EOM approach match exactly with the numerical results obtained from the HEOM method for tier level $L = 3$. The only noticeable difference occurs at large bias ($V = 1$), where the new regions created by the finite bias are flat and stable in the analytical EOM results, while the HEOM predicts non-monotonous behavior of the densities for varying local potentials v_i . In these regions, the HEOM local occupations show increases (or decreases) before continuing to decrease (or increase) again. The corresponding charge current shows a flatter behavior in the EOM results than in the HEOM, where the local

plateaus of high currents is smoother.

Fig. 4 shows the charge and heat currents as functions of the gate voltages (v_1, v_2) for different values of the bias V . The occurrence of regions of finite charge and heat currents can be understood in terms of the poles of the GFs. As explained before, the finite bias contributions in the Fermi functions can be shifted to the poles of the spectral function, giving rise to effective gate levels. Since both the charge and heat current Eq. (4b) depend on the difference between the Fermi functions, the resulting contributions of each pole cancel each other except for the stripe regions. In the left panels of Fig. 4 we show in different colors the contribution of each of the poles defined in Eq. (8) due to the different shift by the left and right bias. These regions exactly correspond to the stripes that appear at finite bias in the stability diagrams. In particular, the $I(p_j)$ correspond to the finite current generated due the contribution of $p_{1,j}$ and $p_{2,j}$ (in the following we use p_j as a collective variable which contains contributions both from $p_{1,j}$ and $p_{2,j}$)

$$I(p_j) = -\frac{\gamma}{2\pi} \sum_{i,\alpha} s_\alpha r_{i,j} \text{Im}[\psi(z_{i,j}^\alpha)]. \quad (15)$$

With this definition, the total current is $I = \sum_j I(p_j)$. In particular, the poles related to site one (two) will generate the stripe regions in the vertical (horizontal) directions in the (v_1, v_2) plane. For instance, the stripe related to the pole $p_{2,2} = v_2 + U_2$ (horizontal blue line in the left panels of Fig. 4) will separate the regions of local occupations $(0, 1)$ and $(0, 2)$, since it exactly corresponds to the energy difference between the respective states. The dark (light) gray squared regions have contributions from both adjacent equal (different) poles. In the central and right panels of Fig. 4 the charge and heat currents are shown for $V = 0.5$ (top panels) and $V = 1$ (bottom panels). The charge current is essentially constant along the stripe regions, with a higher value in the squares where two of the finite pole contributions meet (p_2 and p_5 or p_3 and p_6). In particular, the two dark gray regions adjacent to the region with occupations $n_i = 1$, both local occupations take one of the non-integer values of $3/4$ and $5/4$, and the charge current reaches its maximum value for that given bias. On the other hand, the heat current varies along the perpendicular direction of the stripes, increasing its value as the gate related to the other site is increased. The small finite charge and heat current contributions (in gray) that appear as prolongation of the main structures are effects of the finite coupling strength and they vanish in the limit of small coupling.

In Fig. 5 we plot the total occupation $N = n_1 + n_2$, the charge and the heat currents as functions of the gate and bias at $\delta v = 0$. In the upper left panel of Fig. 5, the lines are solutions of the equations $p_{i,j} - V_\alpha = 0$ where lines with positive (negative) slope correspond to V_L (V_R). Furthermore, the dashed lines correspond to poles $p_{1,j}$ related to site one while the solid lines correspond to poles $p_{2,j}$ related to site two. In the low temperature and low coupling limit, these lines configure the

regions of finite currents (bottom panels of Fig. 5). The main features are three diamonds of vanishing currents which are determined by the intersection of the pole contributions $p_{1,1} = p_{2,1}$, $p_{1,5} = p_{2,5}$, $p_{2,3}$ and $p_{1,4}$. For a fixed bias voltage, a visual interpretation can be obtained if one takes the path determined for fixed δv in the left panels of Fig. 4. As the gates are varied, the transitions between the regions of integer local occupations corresponding to the stripes are crossed. In particular, for $v_1 = v_2$, the stripes transition regions are determined by the aforementioned poles p_1 , p_5 , $p_{2,3}$, and $p_{1,4}$.

In Fig. 6, we present colormaps of the linear transport coefficients and the figure of merit as function of the common gate level $v = v_1 = v_2$ and the inter-dot Coulomb interaction U_{12} at $U_1 = U_2 = 1$, $T = 0.1$ and $\gamma = 0.05$. The overall structure of the transport coefficients is determined by the GF of the system. The conductance exhibits regions of high values determined by straight and diagonal lines in the plane corresponding to the resonance conditions where the energy levels of the DQD align with the Fermi levels of the leads. These resonances are determined by the poles of the GF, following the Coulomb blockade peaks at $p_{i,j} = 0$. The two main poles that contribute at any inter-dot Coulomb repulsion are $p_{i,1}$ and $p_{i,4}$. As the inter-dot interaction is increased above $U_{12} > 1$ the other finite contributions to the conductance peaks originate from the poles $p_{i,5}$ and $p_{i,3}$ to $p_{i,2}$ and $p_{i,6}$. Similarly, the Seebeck coefficient \mathcal{S} , displays a structure of vertical and diagonal bands where \mathcal{S} changes sign, indicating regions of strong thermoelectric response. These bands are aligned along specific directions in the v and U_{12} parameter space, again dictated by the poles of the GF. The highest values of \mathcal{S} , both positive and negative, are observed at the intersections of the lines governed by $p_{i,1}$, $p_{i,4}$, $p_{i,2}$ and $p_{i,6}$. The electronic contribution to the thermal conductance κ_e , shown in Fig. 6(c), also displays a structured pattern with peaks occurring at similar resonance conditions as the conductance and Seebeck coefficient. Interestingly, the highest κ_e values are obtained for inter-Coulomb repulsion around $U_{12} \sim 0.5, 1.5$.

The figure of merit ZT , shown in Fig. 6(d), highlights regions where the system achieves optimal thermoelectric performance. High ZT values are concentrated along the lines of resonance, particularly around $v = 0$, $v = -2U_{12} - U_i$, $v = -U_i$ and $v = -2U_{12}$. For example, at $v \approx 0.2$, ZT reaches a maximum due the combined effects of high \mathcal{S} , moderate \mathcal{G} , and controlled κ_e . These regions signify the potential for efficient thermoelectric energy conversion in the DQD system.

IV. CONCLUSIONS

In this paper, we have presented a fully analytical solution of the equation of motions for an interacting double quantum dot, each symmetrically connected to two leads, in the Coulomb blockade regime out of thermal

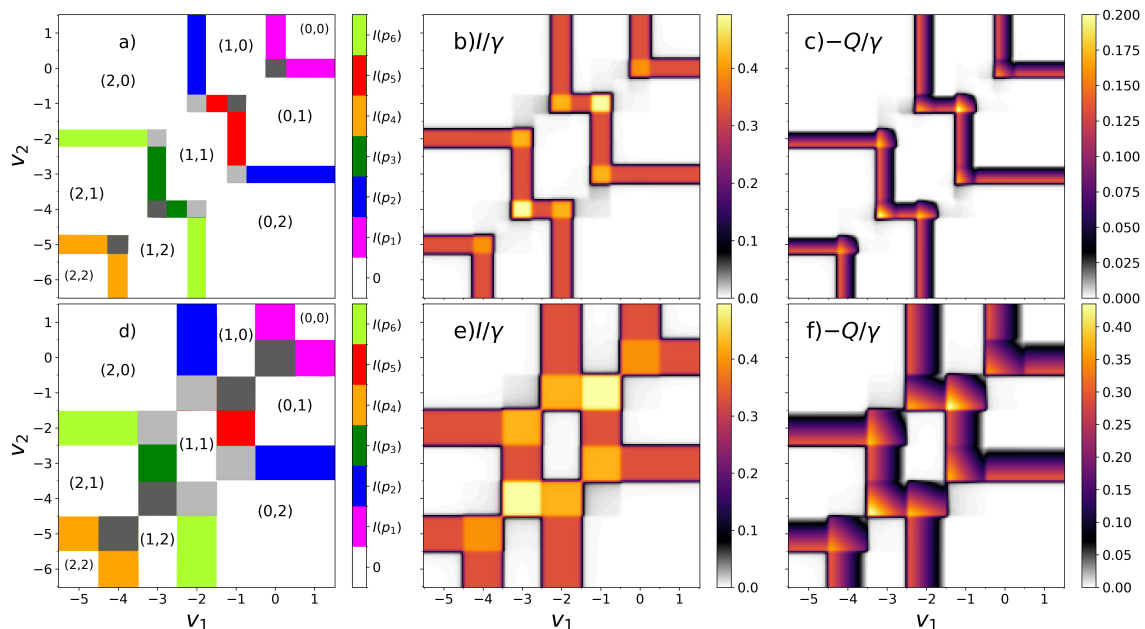


FIG. 4. Charge and heat currents as functions of gate potentials v_i for $V = 0.5$ (top panels) and $V = 1$ (bottom panels). The left panels show the contributions from the poles of the spectral function (Eq. (23) of Ref. [59]) in the regions of finite currents. The other parameter and interaction values are $U_1 = 2$, $U_2 = 3$, $T = 0.02$ and $\gamma = 0.01$. Energies in units of U_{12} .

equilibrium. The one-particle GF is obtained purely in terms of the local occupations and the interactions by solving a linear system for the density correlators analytically, following an equivalent derivation for thermal equilibrium. Our out-of-equilibrium approach has the same formal structure as the equilibrium approach of Ref. [59] with the only difference being that the relation Eq. (5) between (out-of-equilibrium) density correlators and (higher-order) GFs now contains an average of two Fermi functions, each referring to one of the leads. This form alone incorporates all the dependencies on the driving forces and, compared to equilibrium, leads to a single modified definition for the function of Eq. (9). Subsequently, the local occupations, the charge and heat currents, the transport coefficients, and the figure of merit can all be analytically expressed solely in terms of system parameters, interactions, and external driving forces (both bias and temperature gradient).

The evolution of the regions of stable occupations for finite bias is understood in terms of the poles of the one-particle GF of the system, which correspond to the addition and removal energies of the equilibrium situation, shifted due to the bias. The application of a finite bias results in the formation of stripe regions of non-integer local occupations in the plane of the gate levels. These stripe regions exactly define the regions of non-vanishing charge and heat currents in the limit of low coupling and low temperature. The Coulomb blockade diamond structure of the currents in the gate-bias plane is also completely determined by the pole structure of the GF, allowing for an understanding of the far-from-equilibrium properties

of the system under given working conditions.

The analytical results obtained with the EOM method were compared against numerical results obtained with the HEOM technique. Our approach correctly reproduces the emergence of the stripe regions as the bias is increased, accurately capturing the local occupations and the currents along different directions in the plane of the local gate levels and for various out-of-equilibrium configurations in the Coulomb blockade regime, thus validating the approximation of our derivation. Furthermore, our derivation of the linear transport coefficients allowed us to calculate the figure of merit, providing a comprehensive assessment of the thermoelectric performance of the DQD system and identifying regions with efficient thermoelectric energy conversion.

The analytical EOM approach provides significant advantages, including the ability to reveal explicit functional dependencies that elucidate the underlying physical mechanisms of the system. Additionally, this method is computationally efficient, enabling extensive exploration of different parameter regimes and the detailed study of transport properties.

ACKNOWLEDGEMENTS

We acknowledge financial support by grant IT1453-22 “Grupos Consolidados UPV/EHU del Gobierno Vasco” as well as through Grant PID2020-112811GB-I00 funded by MCIN/AEI/10.13039/501100011033. We acknowledge technical

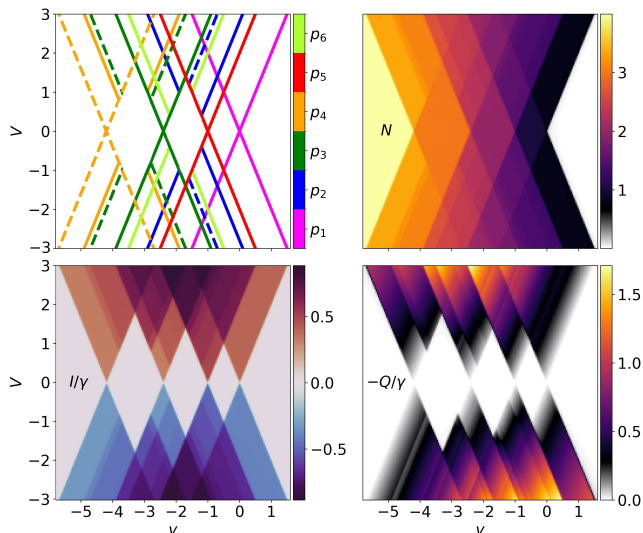


FIG. 5. Top left panel: positions of the poles with significant non-vanishing residues corresponding to solutions of $p_{i,j} - V_\alpha = 0$ with $V_L = -V_R = V/2$ as function of gate $v = v_1 = v_2$ and bias V . The lines with positive (negative) slopes correspond to V_L (V_R), while the solid (dashed) lines correspond to poles related to site two (one). The other panels show the total occupation $N = n_1 + n_2$ (top right), the charge (bottom left) and the heat currents (bottom right). Here the parameters of the model are $U_1 = 2.2$, $U_2 = 1.4$, as well as $T = \gamma = 0.01$. Energies in units of U_{12} .

support provided by SGIker (Scientific Computing Services UPV/EHU). N.S. acknowledges funding from the European Union under the Horizon Europe research and innovation programme (Marie Skłodowska-Curie grant agreement no. 101148213, EATTS). DJ acknowledges funding by the “Plan Gen-T of Excellence” of Generalitat Valenciana through grant CIDEXG/2023/7.

-
- [1] M. S. Dresselhaus, G. Chen, M. Y. Tang, R. Yang, H. Lee, D. Wang, Z. Ren, J.-P. Fleurial, and P. Gogna, New directions for low-dimensional thermoelectric materials, *Adv. Mater.* **19**, 1043 (2007).
- [2] G. J. Snyder and E. S. Toberer, Complex thermoelectric materials, *Nat. Mater.* **7**, 105 (2008).
- [3] L. E. Bell, Cooling, heating, generating power, and recovering waste heat with thermoelectric systems, *Science* **321**, 1457 (2008).
- [4] F. Giazotto, T. T. Heikkilä, A. Luukanen, A. M. Savin, and J. P. Pekola, Opportunities for mesoscopics in thermometry and refrigeration: Physics and applications, *Rev. Mod. Phys.* **78**, 217 (2006).
- [5] M. Zebarjadi, K. Esfarjani, M. S. Dresselhaus, Z. F. Ren, and G. Chen, Perspectives on thermoelectrics: from fundamentals to device applications, *Energy Environ. Sci.* **5**, 5147 (2012).
- [6] A. Shakouri, Recent developments in semiconductor thermoelectric physics and materials, *Annu. Rev. Mater. Res.* **41**, 399 (2011).
- [7] C. J. Vineis, A. Shakouri, A. Majumdar, and M. G. Kanatzidis, Nanostructured thermoelectrics: big efficiency gains from small features, *Adv. Mater.* **22**, 3970 (2010).
- [8] P. Pichanusakorn and P. R. Bandaru, Nanostructured thermoelectrics, *Mater. Sci. Eng. R Rep.* **67**, 19 (2010).
- [9] A. P. Alivisatos, Perspectives on the physical chemistry of semiconductor nanocrystals, *J. Phys. Chem.* **100**, 13226 (1996).
- [10] M. Bayer, G. Ortner, O. Stern, A. Kuther, A. A. Gorbunov, A. Forchel, P. Hawrylak, S. Fafard, K. Hinzer, T. L. Reinecke, *et al.*, Coupling and entangling of quantum states in quantum dot molecules, *Science* **291**, 451 (2001).
- [11] M. A. Kastner, Artificial atoms, *Phys. Today* **46**, 24 (1993).
- [12] M. A. Reed, J. N. Randall, R. J. Aggarwal, R. J. Matyi, T. M. Moore, and A. E. Wetsel, Observation of discrete electronic states in a zero-dimensional semiconductor nanostructure, *Phys. Rev. Letters* **60**, 535 (1988).
- [13] W. G. van der Wiel, S. De Franceschi, J. Elzerman, T. Fujisawa, S. Tarucha, and L. Kouwenhoven, Electron transport through double quantum dots, *Rev. Mod. Phys.* **75**, 1 (2002).
- [14] R. Hanson, L. P. Kouwenhoven, J. R. Petta, S. Tarucha, and L. M. Vandersypen, Spins in few-electron quantum dots, *Rev. Mod. Phys.* **79**, 1217 (2007).
- [15] J. Petta, A. Johnson, J. Taylor, E. Laird, A. Yacoby, M. Lukin, C. Marcus, M. Hanson, and A. Gossard, Coherent manipulation of coupled electron spins in semiconductor quantum dots, *Science* **309**, 2180 (2005).
- [16] S. Juergens, F. Haupt, M. Moskalets, and J. Splettstoesser, Thermoelectric performance of a driven double quantum dot, *Phys. Rev. B* **87**, 245423 (2013).
- [17] S. Donsa, S. Andergassen, and K. Held, Double quantum dot as a minimal thermoelectric generator, *Phys. Rev. B* **89**, 125103 (2014).

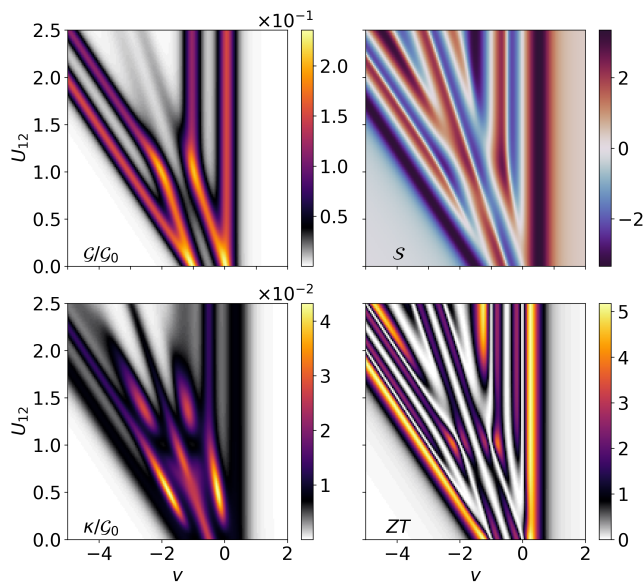


FIG. 6. Linear transport coefficients and figure of merit as a function of the gate level v and the inter-Coulomb repulsion U_{12} for fixed $T = 2\gamma = 0.1$. Energies in units of $U_1 = U_2$.

- [18] N. A. Zimbovskaya, Thermoelectric properties of a double-dot system in serial configuration within the coulomb blockade regime, *J. Chem. Phys.* **153**, 124712 (2020).
- [19] B. R. Pirot, N. R. Abdullah, A. Manolescu, and V. Gudmundsson, Thermal transport controlled by intra-and inter-dot coulomb interactions in sequential and cotunneling serially-coupled double quantum dots, *Physica B* **629**, 413646 (2022).
- [20] J. You and H.-Z. Zheng, Spectral properties of a double-quantum-dot structure: A causal green's function approach, *Phys. Rev. B* **60**, 8727 (1999).
- [21] S. Lamba and S. Joshi, Transport through a coupled quantum dot system: Role of interdot interactions, *Phys. Rev. B* **62**, 1580 (2000).
- [22] R. Žitko, Fano-kondo effect in side-coupled double quantum dots at finite temperatures and the importance of two-stage kondo screening, *Phys. Rev. B* **81**, 115316 (2010).
- [23] A. Georges and Y. Meir, Electronic correlations in transport through coupled quantum dots, *Phys. Rev. Lett.* **82**, 3508 (1999).
- [24] C. Büsser, E. Anda, A. Lima, M. A. Davidovich, and G. Chiappe, Transport in coupled quantum dots: Kondo effect versus antiferromagnetic correlation, *Phys. Rev. B* **62**, 9907 (2000).
- [25] Y. Meir and N. S. Wingreen, Landauer formula for the current through an interacting electron region, *Phys. Rev. Lett.* **68**, 2512 (1992).
- [26] A.-P. Jauho, N. S. Wingreen, and Y. Meir, Time-dependent transport in interacting and noninteracting resonant-tunneling systems, *Phys. Rev. B* **50**, 5528 (1994).
- [27] H. Haug and A.-P. Jauho, *Quantum kinetics in transport and optics of semiconductors*, Vol. 2 (Springer, 2008).
- [28] S. Datta, *Electronic transport in mesoscopic systems* (Cambridge University Press, 1995).
- [29] M. Di Ventra, *Electrical transport in nanoscale systems* (Cambridge University Press, 2013).
- [30] T. J. Levy and E. Rabani, Steady state conductance in a double quantum dot array: The nonequilibrium equation-of-motion green function approach, *J. Chem. Phys.* **138**, 164125 (2013).
- [31] D. Sztenkiel and R. Świrkowicz, Electron transport through double quantum dot system with inter-dot coulomb interaction, *Acta Phys. Pol. A* **111**, 361 (2007).
- [32] D. M.-T. Kuo and Y.-C. Chang, Tunneling current spectroscopy of a nanostructure junction involving multiple energy levels, *Phys. Rev. Lett.* **99**, 086803 (2007).
- [33] T. Pohjola, J. König, M. Salomaa, J. Schmid, H. Schoeller, and G. Schön, Resonant tunneling through a two-level dot and double quantum dots, *Europhys. Lett.* **40**, 189 (1997).
- [34] C. Niu, L.-j. Liu, and T.-h. Lin, Coherent transport through a coupled-quantum-dot system with strong intradot interaction, *Phys. Rev. B* **51**, 5130 (1995).
- [35] Q.-f. Sun and H. Guo, Double quantum dots: Kondo resonance induced by an interdot interaction, *Phys. Rev. B* **66**, 155308 (2002).
- [36] F. Chi and S.-S. Li, Interdot interaction induced zero-bias maximum of the differential conductance in parallel double quantum dots, *J. Appl. Phys.* **99**, 043705 (2006).
- [37] B. R. Pirot, N. R. Abdullah, and A. K. Ahmed, Thermal transport driven by coulomb interactions in quantum dots: Enhancement of thermoelectric and heat currents, *Physica B* **641**, 414108 (2022).
- [38] D. Perez Daroca, P. Roura-Bas, and A. A. Aligia, Thermoelectric properties of a double quantum dot out of equilibrium in kondo and intermediate valence regimes, *Phys. Rev. B* **108**, 155117 (2023).
- [39] Y. Cheng, Z. Li, J. Wei, H.-G. Luo, and H.-Q. Lin, Thermoelectric transport through strongly correlated double quantum dots with kondo resonance, *Phys. Lett. A* **415**, 127657 (2021).
- [40] L. Tesser, B. Bhandari, P. A. Erdman, E. Paladino, R. Fazio, and F. Taddei, Heat rectification through single and coupled quantum dots, *New J. Phys.* **24**, 035001 (2022).
- [41] Y. Tanimura, Numerically “exact” approach to open quantum dynamics: The hierarchical equations of motion (heom), *The Journal of chemical physics* **153**, 020901 (2020).
- [42] K. G. Wilson, The renormalization group: Critical phenomena and the kondo problem, *Rev. Mod. Phys.* **47**, 773 (1975).
- [43] X.-Q. Li, J. Luo, Y.-G. Yang, P. Cui, and Y. Yan, Quantum master-equation approach to quantum transport through mesoscopic systems, *Phys. Rev. B* **71**, 205304 (2005).
- [44] A. Georges, G. Kotliar, W. Krauth, and M. J. Rozenberg, Dynamical mean-field theory of strongly correlated fermion systems and the limit of infinite dimensions, *Rev. Mod. Phys.* **68**, 13 (1996).
- [45] H.-P. Breuer and F. Petruccione, *The Theory of Open Quantum Systems* (Oxford University Press, 2002).
- [46] D. A. Ryndyk, R. Gutiérrez, B. Song, and G. Cuniberti, Green function techniques in the treatment of quantum transport at the molecular scale, in *Energy Transfer Dy-*

- namics in Biomaterial Systems* (Springer Berlin Heidelberg, Berlin, Heidelberg, 2009) pp. 213–335.
- [47] D. N. Zubarev, Double-time green functions in statistical physics, *Sov. Phys. Usp.* **3**, 320 (1960).
- [48] J. Hubbard, Electron correlations in narrow energy bands, *Proc. R. Soc. Lond. A* **276**, 238 (1963).
- [49] J. Hubbard, Electron correlations in narrow energy bands. ii. the degenerate band case, *Proc. R. Soc. Lond. A* **277**, 237 (1964).
- [50] J. Hubbard, Electron correlations in narrow energy bands iii. an improved solution, *Proc. R. Soc. Lond. A* **281**, 401 (1964).
- [51] Y. Meir and N. S. Wingreen, Landauer formula for the current through an interacting electron region, *Phys. Rev. Lett.* **68**, 2512 (1992).
- [52] K. Kang and B. Min, Equation-of-motion treatment of the impurity anderson model with a finite on-site coulomb repulsion, *Phys. Rev. B* **52**, 10689 (1995).
- [53] R. Van Roermund, S.-y. Shiao, and M. Lavagna, Anderson model out of equilibrium: Decoherence effects in transport through a quantum dot, *Phys. Rev. B* **81**, 165115 (2010).
- [54] K. Kang, Transport through an interacting quantum dot coupled to two superconducting leads, *Phys. Rev. B* **57**, 11891 (1998).
- [55] R. Świrkowicz, J. Barnaś, and M. Wilczyński, Nonequilibrium kondo effect in quantum dots, *Phys. Rev. B* **68**, 195318 (2003).
- [56] M. A. Sierra, M. Saiz-Bretín, F. Domínguez-Adame, and D. Sánchez, Interactions and thermoelectric effects in a parallel-coupled double quantum dot, *Phys. Rev. B* **93**, 235452 (2016).
- [57] M. I. Alomar, J. S. Lim, and D. Sánchez, Coulomb-blockade effect in nonlinear mesoscopic capacitors, *Phys. Rev. B* **94**, 165425 (2016).
- [58] Y.-C. Chang and D. M.-T. Kuo, Theory of charge transport in a quantum dot tunnel junction with multiple energy levels, *Phys. Rev. B* **77**, 245412 (2008).
- [59] N. Sobrino, D. Jacob, and S. Kurth, Fully analytical equation of motion approach for the double quantum dot in the coulomb blockade regime, *Phys. Rev. B* **110**, 115121 (2024).
- [60] M. F. Ludovico, J. S. Lim, M. Moskalets, L. Arrachea, and D. Sánchez, Dynamical energy transfer in ac-driven quantum systems, *Phys. Rev. B* **89**, 161306 (2014).
- [61] B. R. Bulka and T. Kostyrko, Electronic correlations in coherent transport through a two quantum dot system, *Phys. Rev. B* **70**, 205333 (2004).
- [62] D. M.-T. Kuo, S.-Y. Shiao, and Y.-c. Chang, Theory of spin blockade, charge ratchet effect, and thermoelectrical behavior in serially coupled quantum dot system, *Phys. Rev. B* **84**, 245303 (2011).
- [63] D. M. T Kuo and Y.-C. Chang, Effects of interdot hopping and coulomb blockade on the thermoelectric properties of serially coupled quantum dots, *Nanoscale Res. Lett.* **7**, 1 (2012).
- [64] N. Sobrino, F. Eich, G. Stefanucci, R. D’Agosta, and S. Kurth, Thermoelectric transport within density functional theory, *Phys. Rev. B* **104**, 125115 (2021).
- [65] L. Onsager, Reciprocal relations in irreversible processes. i., *Phys. Rev.* **37**, 405 (1931).
- [66] M. Abramowitz and I. A. Stegun, *Handbook of mathematical functions with formulas, graphs, and mathematical tables*, Vol. 55 (US Government printing office, 1968).
- [67] N. Sobrino, S. Kurth, and D. Jacob, Exchange-correlation potentials for multiorbital quantum dots subject to generic density-density interactions and hund’s rule coupling, *Phys. Rev. B* **102**, 035159 (2020).
- [68] N. Sobrino, EOM.DQD, https://github.com/Nahualcsc/EOM_DQD (2024).
- [69] G. Stefanucci and S. Kurth, Steady-state density functional theory for finite bias conductances, *Nano Lett.* **15**, 8020 (2015).